



● *Original Contribution*

NON-LINEAR ACOUSTIC EMISSIONS FROM THERAPEUTICALLY DRIVEN CONTRAST AGENT MICROBUBBLES

JAE HEE SONG,* ALEXANDRU MOLDOVAN,[†] and PAUL PRENTICE*

* CavLab, Medical and Industrial Ultrasonics, University of Glasgow, Glasgow, United Kingdom; and [†] Centre for Ultrasound Engineering, University of Strathclyde, Glasgow, United Kingdom

(Received 29 August 2018; revised 25 March 2019; in final form 1 April 2019)

Abstract—Non-linear emissions from microbubbles introduced to the vasculature for exposure to focused ultrasound are routinely monitored for assessment of therapy and avoidance of irreversible tissue damage. Yet the bubble-based mechanistic source for these emissions, under subresonant driving at typical therapeutic pressure amplitudes, may not be well understood. In the study described here, dual-perspective high-speed imaging at 210,000 frames per second (fps), and shadowgraphically at 10 Mfps, was used to observe cavitation from microbubbles flowing through a 500- μm polycarbonate capillary exposed to focused ultrasound of 692 kHz at therapeutically relevant pressure amplitudes. The acoustic emissions were simultaneously collected *via* a broadband calibrated needle hydrophone system. The observations indicate that periodic bubble-collapse shock waves can dominate the non-linear acoustic emissions, including subharmonics at higher driving amplitudes. Contributions to broadband emissions through variance in shock wave amplitude and emission timings are also identified. Possible implications for *in vivo* microbubble cavitation detection, mechanisms of therapy and the conventional classification of cavitation activity as stable or inertial are discussed. (E-mail: paul.prentice@glasgow.ac.uk) © 2019 The Author(s). Published by Elsevier Inc. on behalf of World Federation for Ultrasound in Medicine & Biology. This is an open access article under the CC BY license. (<http://creativecommons.org/licenses/by/4.0/>).

Key Words: Microbubble, Cavitation, Focused ultrasound, Acoustic emissions, Bubble collapse, Shock wave.

INTRODUCTION

During the application of focused ultrasound for tissue disruption and drug delivery, contrast agent microbubble suspensions are often injected into the vasculature to mediate therapy (Ferrara et al. 2007). Non-linear acoustic emissions generated by the driven microbubbles are routinely monitored for assessment of therapeutic bio-effect. This is particularly the case for applications in which avoidance of overtreatment is critical, such as transcranial blood–brain barrier disruption, for which recent clinical (Lipsman et al. 2018) and extensive pre-clinical (Jones et al. 2018; O’Reilly and Hynynen 2012; Sun et al. 2017; Wu et al. 2014) development is underway. With typical focused ultrasound fundamental driving frequencies (f_0) of several hundreds of kilohertz employed, for sufficient transmission across the skull,

various combinations of harmonic emissions at nf_0 (where n is any integer), subharmonics at $nf_0/2$ and broadband emissions are commonly reported. Generally for therapeutic applications, harmonic emissions are associated with lower driving amplitudes, with higher threshold values required for subharmonic and broadband emissions (Jones et al. 2018; McDannold et al. 2006). Indeed, rapid control feedback loops modulating the driving amplitude in response to non-linear emission components (O’Reilly and Hynynen 2012; Sun et al. 2017) may be an important technology for safe clinical realisation of microbubble-mediated therapy of the brain.

A volume of literature exists detailing direct observation of microbubbles *via* high-speed optical imaging, under higher driving frequencies typical of diagnostic imaging, close to or above microbubble resonance. This research aims to identify sources of non-linear emissions responsible for contrast enhancement, the original application for microbubble suspensions in medical ultrasound. A range of microbubble behaviour such as

Address correspondence to: Paul Prentice, Cavitation Research Laboratory, James Watt South Building, School of Engineering, University of Glasgow, Glasgow G12 8QQ, UK. E-mail: paul.prentice@glasgow.ac.uk

compression-only (de Jong *et al.* 2007; Sijl *et al.* 2011) and non-spherical oscillations (Dollet *et al.* 2008; Versluis *et al.* 2010) have been proposed as sources of non-linear emissions, including spherical period-doubling (Chomas *et al.* 2002) and subharmonic (Sijl *et al.* 2010) responses for driving at around twice microbubble resonance. These studies, however, lacked parallel acoustic monitoring for verification that the identified behaviour translated to a detectable component within the acoustic emissions.

Other reports on high-speed imaging of microbubbles, driven at lower frequencies (≤ 1 MHz) and pressure amplitudes typical of those used for therapy (Caskey *et al.* 2007; Chen *et al.* 2011a, 2011b; Lajoine *et al.* 2018; Prentice *et al.* 2005; van Wamel *et al.* 2006), seek primarily to identify mechanisms of tissue disruption and drug delivery. Potential mechanistic sources for non-linear emissions under such driving conditions, however, are not so well addressed. Clearly, a robust understanding of the source of non-linear emissions from microbubbles driven below resonance would aid detection and monitoring of therapy, and may also provide insights into the mechanisms underpinning tissue disruption and drug delivery.

Here, we report on observations from diluted samples of SonoVue contrast agent microbubbles flowing through a 500- μm polycarbonate capillary, driven by a 200-cycle burst of 692-kHz focused ultrasound, at peak-negative pressure (PNP) amplitudes ranging from 385–1.14 MPa. The capillary is mounted at 45° relative to the axis of focused ultrasound propagation, to facilitate dual high-speed imaging from orthogonal perspectives, represented schematically in Figure 1a. Top-view imaging is recorded at 210,000 frames per second (fps) for the duration of the focused ultrasound exposure. Side-view imaging is captured at 10 Mfps for a duration of 25.6 μs , from ~ 65 μs after focused ultrasound has propagated to the capillary. Side-view illumination is provided by collimated synchronous 10-ns laser pulses, for shadowgraphic imaging of acoustic transients as they propagate through the field of view (FOV). Acoustic emissions from the imaged microbubble cavitation are sampled *via* a broadband calibrated needle hydrophone system, with the sensing tip located within 100 μm from the capillary outer wall, such that it is visible in both imaging FOVs. Acoustic data are presented in time and frequency domain, deconvolved from the impulse response of the hydrophone over a representative bandwidth and filtered, as described below.

METHODS

Experimental configuration

A focused ultrasound transducer (H-149, Sonic Concepts, Bothell, WA, USA), excited by a waveform

generator (DG4102, Rigol Technologies, Beijing, China) and a power amplifier (2100 L, Electronics and Innovation, Rochester, NY, USA), was mounted in a chamber on an *xyz* manipulator (Velmex Motor, Bloomfield, NY, USA). The transducer has an outer diameter of 110 mm, and geometrically focuses to 68 mm from the front face. The field generated propagates horizontally in the *x*-direction of a chamber, measuring 420 \times 438 \times 220 mm³, that also features two recessed opposing walls (along the *z*-axis), to allow positioning of optics for reasonably high spatial resolution imaging (side view, described below). The chamber was filled with de-ionised water, degassed *via* boiling and cooling in sealed containers, to < 4 mg/L dissolved oxygen.

A polycarbonate capillary (inner/outer diameter 500 μm /550 μm , Paradigm Optics, Vancouver, WA, USA) was mounted into the chamber *via* a custom 3-D printed support, such that the capillary was located at the acoustic focus, at 45° to the propagation axis and in the horizontal plane (Fig. 1a). PNP amplitude measurements at the focus with the 0.2-mm polyvinyl difluoride needle hydrophone (fully described below, but for focused ultrasound characterisation measurements, aligned to the axis of propagation), with and without the capillary in position, indicated attenuation of $< 5\%$ across the PNPs stated in the Results, with free-field measurements reported. All observations were taken over a 200-cycle burst of 692-kHz focused ultrasound (~ 289 μs), operating at the third harmonic of the transducer, with initial excitation denoting $t = 0$ μs . Use of the third harmonic also introduced a transition response for the focused ultrasound generated to ramp up to the required PNP amplitude, with measurements indicating ~ 16 μs to achieve 90% of the value stated. The significant harmonic components from non-linear propagation of the focused ultrasound, at each PNP reported, are illustrated in Figure 1b and summarized in Table 1, for 459 kPa.

SonoVue (Bracco, Milan Italy) is a commercial ultrasound contrast agent consisting of phospholipid-shelled sulphur hexafluoride gas-core microbubbles, with a mean diameter between 2 and 3 μm (95% < 10 μm), and associated resonance frequencies > 2 MHz, dependent on initial microbubble diameter (van der Meer *et al.* 2004). SonoVue suspensions at an initial concentration of 100–500 million/mL (Schneider 1999) were prepared according to manufacturer's guidance and subsequently diluted by a factor of $\sim 1:80,000$ in (non-degassed) de-ionised water, using a syringe. A new phial of SonoVue was used for each day of experimental acquisition, with fresh diluted samples prepared from it on an hourly basis. A series of preliminary experiments were also conducted using saline as the dilution medium. Microbubble cavitation activity observations equivalent to those presented in the Results

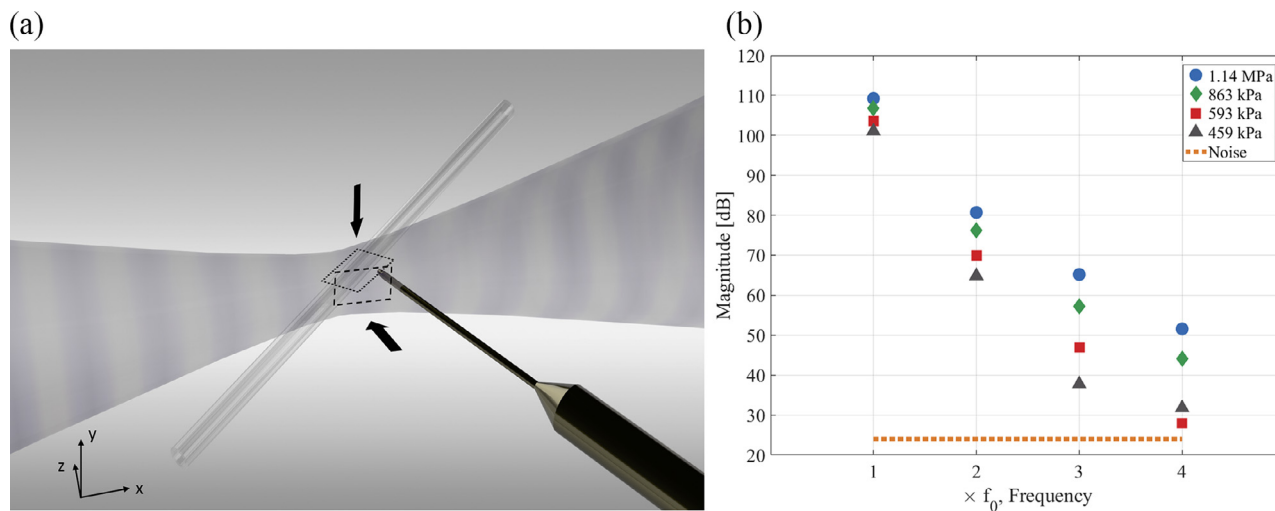


Fig. 1. (a) Schematic representation of the experimental configuration, depicting exposure of the capillary, orientated in the horizontal plane at 45° to the focused ultrasound, and the needle hydrophone in the emission collection position. Focused ultrasound propagates from left to right, and microbubble flow was from back right to front left, for this representation. The imaging axis and fields of view for the high-speed imaging are also represented (top view *dotted*, side view *dashed*). (b) Assessment of focused ultrasound propagation non-linearity, up to $4f_0$ for the peak-negative pressure amplitudes reported in the Results.

(according to PNP) suggested that microbubbles are reasonably stable, in water, over this time scale. The syringe was then connected to a 20G microlance (~ 0.6 -mm internal diameter), with one end of the capillary epoxied within the bore of the lance and mounted into a syringe pump (74900, Cole Parmer, Cambridgeshire UK), set to fixed flow rate of 7.5 mL/h. The exhaust end of the capillary was vented to a collection reservoir located outside the chamber.

Dual high-speed imaging

High-speed imaging was conducted along the vertical y-axis (top-view) and horizontal z-axis (side-view), orthogonally to the axis of focused ultrasound propagation. Top-view imaging was captured through a long-working-distance objective lens (5×0.14 Numerical Aperture (NA), focal length (in air): 40.0 mm Mitutoyo, Kawasaki Japan) in a sealed watertight casing, with a Fastcam SA-Z 2100 K (Photron, Bucks UK) at 210,000 fps and shutter time of 159 ns, for the duration of the

Table 1. Relative magnitudes of focused ultrasound non-linear propagation harmonics at 459 kPa (Fig. 1b) and spectral harmonic components from microbubble-cavitation driven at a PNP of 459 kPa (Fig. 4c, dark grey)

	Harmonic magnitude (dB)			
	f_0	$2f_0$	$3f_0$	$4f_0$
Focused ultrasound at PNP = 459 kPa	101.1	64.82	37.75	31.79
Microbubble cavitation emission spectrum	136.5	105.3	91.92	89.95

PNP = peak-negative pressure.

focused ultrasound exposure. At this frame rate, images are formed over 384×160 pixels with a spatial resolution of $4.2 \mu\text{m}/\text{pixel}$, which is insufficient to resolve the majority of quiescent microbubbles, before focused ultrasound excitation. The FOV, represented by the *dotted rectangle* in Figure 1a, however, covers the width and ~ 1.5 mm of the length of the capillary within the acoustic focus, to ensure that the needle hydrophone, in the position represented in Figure 1a, detected only emissions generated by imaged microbubble cavitation, during the focused ultrasound exposure. Before, and during data acquisition, the vertical positioning of the objective lens was adjusted to obtain focus on the capillary walls at their widest point. Illumination for top-view imaging was provided by a continuous 150-W halogen bulb light source (Thorlabs, Ely UK), coupled to a liquid light guide, with the output end located ~ 10 mm below the capillary (not shown, Fig. 1a). Figure 2c depicts 7.5 ± 0.2 - μm -diameter polymer microspheres (PS06005, Bangs Laboratories, IN, USA), imaged through the top-view configuration at full FOV, for further indication of resolution.

Side-view imaging, with the FOV represented as a dashed rectangle in Figure 1a, was undertaken through a Monozoom 7 lens (Bausch & Lomb, Rochester, NY, USA) at 10 Mfps with a Shimadzu HPV-X2 camera (Shimadzu, Kyoto Japan) over a 25.6 - μs duration from $t = 125 \mu\text{s}$, such that microbubble cavitation has evolved over ~ 45 cycles of focused ultrasound driving. Illumination was achieved with synchronous (to frame capture) 10-ns laser pulses (CAVILUX Smart, Cavitar, Tampere, Finland), coupled to a liquid light guide and collimating

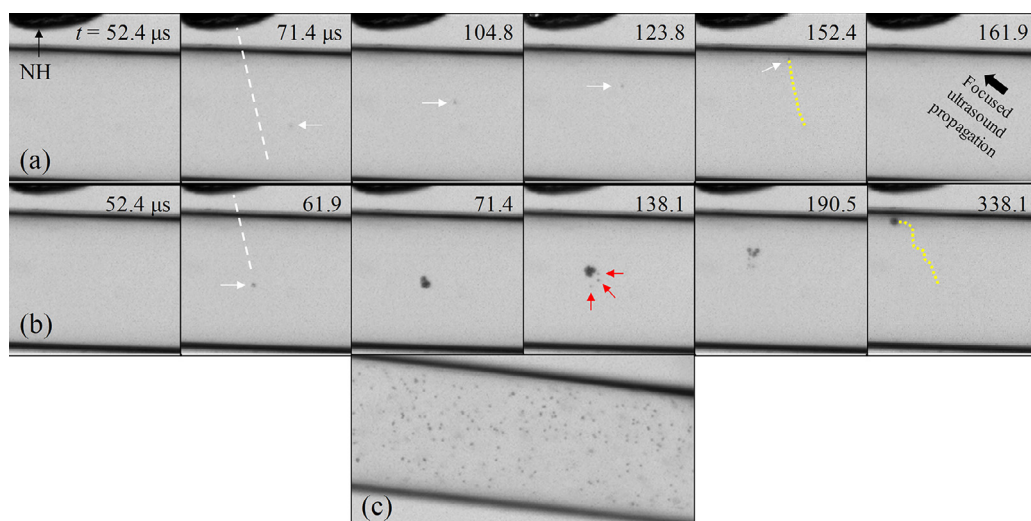


Fig. 2. Representative images extracted from a top-view sequence captured at 210 kfps, from $t = 0 \mu\text{s}$ for the duration of the focused ultrasound exposure, of microbubble cavitation activity driven by peak-negative pressures of (a) 459 kPa and (b) 1.14 MPa. Scale is provided by the 500- μm internal diameter of the capillary, flow is from left to right and the tip of the needle hydrophone (*arrowed NH*) is visible to the top left of each image, with the axis of the needle represented (*white dashed line*, second frame). Focused ultrasound propagation direction is depicted at 161.9 μs in (a), with triggering of focused ultrasound defined as $t = 0 \mu\text{s}$, and propagation time to the capillary = 51.6 μs . (c) 7.5- μm -diameter polymer microspheres, under equivalent imaging conditions and flow conditions, for indication of resolution.

lens. This configuration facilitates shadowgraphic imaging such that pressure transients can be directly visualised *via* refractive index variations imposed as the transient propagates. Note that the duration of side-view capture is apparent in the full-sequence videos of top-view imaging, as the pulsed laser illumination reflects off the bevelled tip of the needle hydrophone. Empirically, we have found that the optimal plane of focus for imaging acoustic transients (Kudo 2015), whilst retaining a perception of cavitation dynamics, is achievable by defocusing the monozoom lens by $\sim 1.5 \text{ mm}$, such that the bubble itself is slightly out of focus during side-view capture (Song *et al.* 2016). The FOV for this perspective was selected to ensure all bubble-collapse shock waves from microbubble cavitation were captured before propagating beyond the imaged region, according to a 0.1- μs frame-to-frame interval. We also note that the collimated laser illumination introduces a limb effect to the imaging of the capillary, whereby the capillary wall appears much larger than the physical 25- μm thickness (see Supplementary videos S3 and S4, at full FOV). Although smaller-internal-diameter capillaries are available, they tend to have similar wall thicknesses such that the limb effect would obscure microbubble cavitation imaging.

Acoustic detection

The acoustic emissions from the driven microbubble cavitation activity were sampled with a 0.2-mm polyvinyl difluoride needle hydrophone (Precision Acoustics, Dorchester, UK), with sensitivity and phase calibration from

100 kHz–20 MHz in 25-kHz increments (National Physical Laboratory, Teddington, UK, November 2017). There is a $\pm 9\%$ magnitude uncertainty associated with the calibration, across the frequency ranges reported, including the measurements of focused ultrasound PNP amplitude. Voltage data from the needle hydrophone system were amplified by $\sim 25 \text{ dB}$ (Hydrophone Amplifier, Precision Acoustics) and collected, for the duration of the focused ultrasound exposure, to an oscilloscope (MS07104 A, Agilent Technologies, Lexington, MA, USA), at 4 Giga-samples (GS)/s. Triggering and synchronisation of all instrumentation was achieved with a delay generator (DG535, Stanford Research Systems, Sunnyvale, CA, USA).

During the experiments, the needle hydrophone was mounted on an xyz micro-manipulator (M-652, Newport, Oxfordshire UK) such that the tip could be positioned $\sim 100 \mu\text{m}$ from the outer capillary wall, with the needle shaft $\sim 15^\circ$ from orthogonal to the capillary axis and $\sim 20^\circ$ below the horizontal plane. This angle of approach was necessary to facilitate imaging from the two perspectives described and because of the physical constraint of the recessed side wall of the chamber architecture. The needle hydrophone tip effectively defined the target region of interest for detectable microbubble activity, within the capillary, on incidence of focused ultrasound.

All single microbubble cavitation time domain data are presented from ~ 60 –175 μs , with the needle hydrophone (in field characterisation position, with the tip located at the capillary position), indicating a propagation

time from the transducer of $51.6 \mu\text{s}$. The impulse response of the needle hydrophone has been deconvolved from the voltage data over a selected bandwidth of 2.4 ($\sim 7f_0/2$) to 20 MHz. This removes the fundamental frequency of the focused ultrasound and significant non-linear components, for revealing shock wave content and restoring an approximation to the physical pressure data (Johansen et al. 2017). Frequency spectra are generated via application of a fast Fourier transform and Hanning window to the time interval presented, but deconvolved across the full calibration bandwidth of 100 kHz–20 MHz, and thereby include the focused ultrasound driving as well as microbubble cavitation emission components.

The experiment described was repeated at each focused ultrasound PNP amplitude reported, until data were recorded from a single microbubble within the target region of the capillary, defined by the tip of the needle hydrophone, and with the ensuing cavitation activity reasonably in focus for the top-view imaging (close to the central horizontal plane of the capillary). We note that needle hydrophone detection of non-linear signals, other than those attributable to the focused ultrasound propagation (Fig. 1b), were consistently accompanied by observable microbubble cavitation activity in the high-speed imaging from both perspectives (and vice versa), initiating from focused ultrasound incidence to the capillary, at the required PNP. Sham exposures conducted regularly during data collection, for which microbubbles were not introduced to the flow, and at PNP values in excess of those at which results are presented below, confirmed that no cavitation activity was observed, or acoustically detected, in the absence of microbubbles.

RESULTS

f_0 and $f_0/2$ shock wave emission regimes

In Figure 2 are representative top-view images of single-microbubble cavitation behaviour, driven with focused ultrasound of PNPs (a) 459 kPa and (b) 1.14 MPa (full image sequence at full FOV, available as Supplementary videos S1 and S2, respectively, online only). Images up to and including the focused ultrasound incidence to the capillary, at $51.6 \mu\text{s}$, indicate that no microbubbles of initial quiescent size larger than the spatial resolution of this perspective are flowing within the capillary. It is only once the pressure amplitude has ramped up sufficiently, during the $\sim 16\text{-}\mu\text{s}$ transition response associated with driving the transducer at its third harmonic (see Methods), that the microbubble cavitation becomes observable in the imaging, at (a) $71.4 \mu\text{s}$ and (b) $61.9 \mu\text{s}$ for PNP = 459 kPa and 1.14 MPa, respectively. This suggests that the focused ultrasound induces cavitation from subresonant microbubbles, likely typical

of the SonoVue population (van der Meer et al. 2004). We also note that we occasionally observed larger microbubbles flowing through the capillary, immediately after sample preparation, during “live” imaging. For high-speed imaging acquisition, however, cavitation was always initiated from unresolved microbubbles. We postulate that buoyancy within the syringe prevented larger microbubbles from entering the capillary, soon after sample preparation. Because of the angle of focused ultrasound incidence to the capillary (Fig. 1a), the primary radiation force of the exposure acts to translate the microbubble cavitation activity at $\sim 45^\circ$, relative to the axis of the capillary, and in the general direction of the needle hydrophone tip. The capillary wall distal to the transducer, however, may also be expected to influence the trajectory of cavitation translation as it is approached.

Within the limit of the temporal resolution of the top-view imaging (see Methods), the microbubble driven at a PNP of 459 kPa shows no indication of fragmentation and translates with an average speed of $\sim 3.4 \text{ m/s}$ (sampled between $70\text{--}150 \mu\text{s}$), into contact with the distal capillary wall at $\sim 152 \mu\text{s}$. No further bubble activity is observed for the rest of the imaging sequence after contact, although it is possible that curvature of the capillary wall obscures any bubble from view. In contrast, the microbubble driven by 1.14 MPa fragments within the first few cycles of driving. Bubble debris trailing the cloud translation, such as that arrowed at $138.1 \mu\text{s}$, was commonly observed from both imaging perspectives, at higher PNP amplitudes. Cloud translation is at a reduced average speed of $\sim 1.1 \text{ m/s}$, possibly because of higher drag forces acting during the larger inflation phases (Johnston et al. 2014), until contact with the distal capillary wall at $\sim 280 \mu\text{s}$. Subsequent translation continues along the inner capillary wall, until the end of the focused ultrasound burst.

In Figure 3(a, b) are representative images from the side-view shadowgraphic sequence, over two consecutive cycles of driving, of the bubble activity captured from top-view in Figure 2(a, b), respectively. These images (and those of the full sequence, over ~ 17 cycles, at full FOV; Supplementary Videos S3 and S4, online only) have been background-subtracted, with a sequence recorded immediately after the bubble activity was captured, but with no focused ultrasound generated, for the purpose of enhancing shadowgraphic features. Figure 3a, of the microbubble driven at 459 kPa, further suggests that the resulting cavitation initiated from a single microbubble, and did not fragment, with apparently radial oscillations in phase with the driving. Figure 3b illustrates the behaviour of the cavitation cloud resulting from the microbubble driven by a PNP of 1.14 MPa. The pressure phases of the focused ultrasound driving at the acoustic focus are apparent from the background

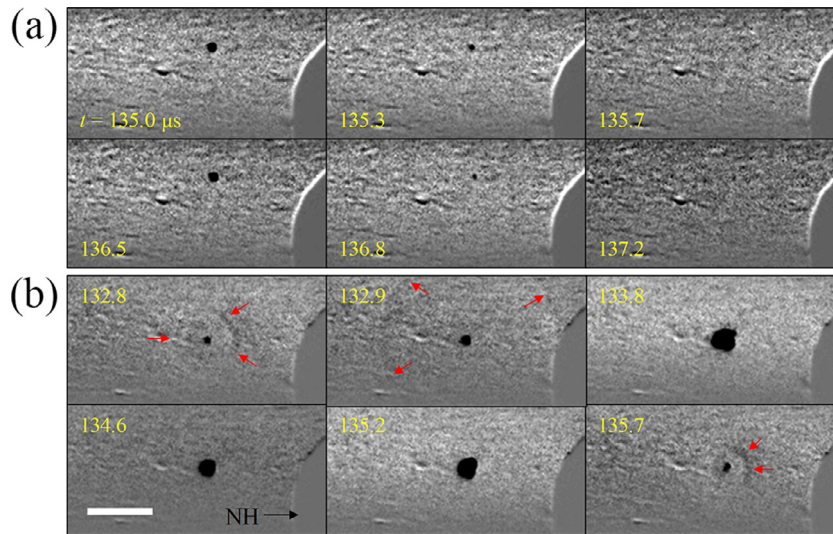


Fig. 3. Images extracted from the side-view shadowgraphic sequence at 10 Mfps, from $t = 125 \mu\text{s}$, of the microbubble cavitation activity also represented from top-view imaging in Figure 2. Flow is from right to left and out of plane. Images are background-subtracted to enhance shadowgraphic features, including focused ultrasound driving and bubble collapse shock waves, *arrowed red* (b). Bar = $150 \mu\text{m}$; however, the cavitation activity appears larger as the imaging is purposefully defocused for shadowgraphic capability.

brightness, with rarefactions (133.8 and $135.2 \mu\text{s}$) presenting as brighter, and compressions ($134.6 \mu\text{s}$) as darker. This effect is particularly prominent in the video version of the full image sequence (Supplementary Video S4, online only). The cloud exhibits overall oscillations at f_0 of the driving, but only collapses strongly enough to emit a shock wave for every other compression, with the same shock wave arrowed at 132.8 and $132.9 \mu\text{s}$, and that from the next collapse, arrowed at $135.7 \mu\text{s}$, $\sim 2/f_0$ later. The deflation in response to the intermediate compression is captured at $134.6 \mu\text{s}$. The creation of bubble debris after collapse, usually to the left of the main cloud in accordance with the direction from which the focused ultrasound has propagated, and re-merging with the cloud over the subsequent cycle are also apparent.

Figure 4(a, b) illustrates the microbubble cavitation acoustic emission data recorded by the needle hydrophone during the high-speed observations of Figures 1 and 2, filtered and hydrophone deconvolved to reveal and restore shock wave features, as described under *Methods*. Figure 4a clearly illustrates periodic shock wave emission at f_0 , consistent with the observation of full oscillations in-phase with the focused ultrasound driving (Fig. 3a). The gradual increase in peak-positive pressure amplitudes of the shock waves, over the first $\sim 30 \mu\text{s}$ of focused ultrasound, may in part be due to the primary radiation force-induced translation of the bubble toward the needle hydrophone tip (Fig. 1a). Notably, shock wave emission ceases at $\sim 158 \mu\text{s}$, corresponding to bubble contact with the capillary wall, indicating that the bubble does not survive the interaction, despite the

focused ultrasound exposure continuing up to $\sim 350 \mu\text{s}$. The spectrum of the signal, *dark grey* in Figure 4c, is hydrophone deconvolved over the calibration bandwidth ($100 \text{ kHz} - 20 \text{ MHz}$) and therefore inclusive of the focused ultrasound. It features peaks at nf_0 reducing in magnitude with increasing frequency, and a noise floor at $\sim 60 \text{ dB}$, close to instrumental noise for the needle hydrophone system, sampled before focused ultrasound incidence to the capillary (*orange dot*). Table 1 details the harmonic magnitudes up to $4f_0$ for the spectrum, relative to the respective value of the non-linear focused ultrasound driving, at 459 kPa (Fig. 1b), indicating the spectral contribution of f_0 -periodic shock waves.

The acoustic emission data for the microbubble cavitation driven at 1.14 MPa (Fig. 4b) indicates that the bubble initially responds with f_0 -shock wave emission, including for a limited duration after fragmentation. Shock waves emitted at $f_0/2$ are apparent from $\sim 70 \mu\text{s}$, confirming the side-view observation of Figure 3b, for emission from cloud collapse during alternate compressional phases, of every other cycle of focused ultrasound.

The shock waves shadowgraphically imaged in Figure 3b are also arrowed within the *dotted rectangle*, which represents the time interval over which side-view imaging was captured. The shock wave peak-positive pressure amplitudes are notably both higher and more variable than the f_0 -emitted shock waves of Figure 4a, such that no clear trend as the cloud translates toward the needle hydrophone tip is apparent. The spectrum of the emission signal (Fig. 4c, *blue*) contains peaks at $nf_0/2$ for all n and a higher noise floor at $\sim 85 \text{ dB}$. Figure 4d

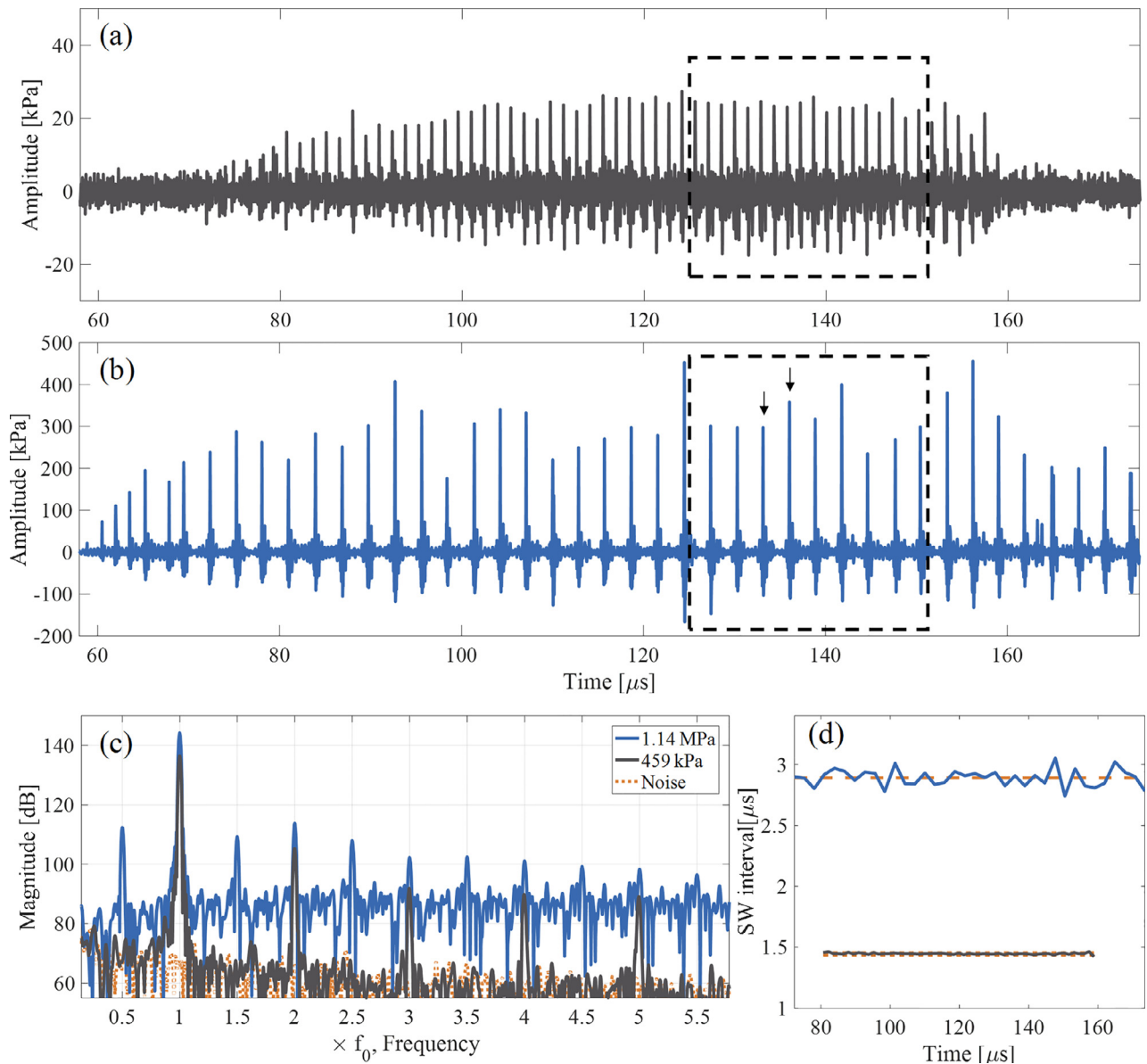


Fig. 4. (a, b) Needle hydrophone data, filtered and deconvolved from 2.4 to 20 MHz, to reveal shock wave content within the microbubble cavitation emission signal, from the activity imaged in Figures 2 and 3 at PNP = 459 kPa and 1.14 MPa, respectively. *Black-dash boxes* correspond to the duration of the shadowgraphic imaging of Figure 3, with shock waves *arrowed* in Figure 3b similarly identified in (b). (c) The spectra of the signal collected, deconvolved from 100 kHz to 20 MHz, thereby including focused ultrasound driving. The needle hydrophone instrumental noise floor is also depicted (*orange dot*). (d) Variance in shock wave emission interval times measured from (a) and (b).

graphically illustrates the variance in shock wave interval timings— $1.448 \pm 0.006 \mu\text{s}$ at 459 kPa and $2.890 \pm 0.073 \mu\text{s}$ at 1.14 MPa (average \pm standard deviation)—over the duration of the focused ultrasound burst, relative to the period of the driving, $1/f_0 \approx 1.45 \mu\text{s}$ and $2/f_0 \approx 2.90 \mu\text{s}$ (*orange dash*).

Synthetic spectral analysis

In this section we provide analysis for both microbubble cavitation noise spectra of Figure 4c, adopting

the *synthetic spectrum* technique (Song et al. 2016, 2017), which facilitates identification of the source of spectral features mediated by periodic shock wave characteristics. Briefly, a simulated bubble-collapse shock wave is modelled *via* the Gilmore equation (Kreider et al. 2011) for a freely collapsing bubble (under ambient atmospheric pressure, with no applied acoustic driving) in water, of maximum radius $R_{\text{max}} = 50 \mu\text{m}$ and equilibrium radius $R_0 = 4.4 \mu\text{m}$, and approximating the emission as a spherically propagating wave. The simulated

shock wave profile is bandpass filtered from 100 kHz–20 MHz, according to the calibration bandwidth of the needle hydrophone. The resulting profile can then be manually fitted, in terms of amplitude and timing, relative to the experimentally detected shock waves.

We note that the R_0 of the simulated bubble does not directly represent the unknown initial size of the SonoVue microbubble, which is unresolved by top-view imaging before focused ultrasound excitation (Fig. 2a, b). The synthetic signal reconstructions described below, of the experimentally detected emission signal, which can vary significantly over the duration of the focused ultrasound exposures including around fragmentation events, is reasonably insensitive to the simulated bubble-collapse parameters, particularly after filtering and within the bandwidths presented.

A reference shock wave is selected as the first detected within the side-view imaging duration, from $t = 125 \mu\text{s}$, for the f_0 and $f_0/2$ shock wave emission regimes at PNPs of 459 kPa and 1.14 MPa, within the *dashed boxes* of Figure 4(a, b), respectively. Various synthetic shock wave trains are constructed in the time domain, around the reference shock wave, as described below. A fast Fourier transform is then applied, consistent with the procedure for generating the spectra of the experimentally detected emission signals, to produce the corresponding synthetic spectrum.

- No variances (*green dot*): Simulated shock waves are assigned a constant peak-positive amplitude, taken as the average over all those experimentally measured within the stable emission duration for each regime, and placed at $1/f_0$ (1.445 μs) or $2/f_0$ (2.890 μs) time intervals as appropriate, relative to the experimentally measured reference shock wave timing.
- Amplitude variance (*orange dot*): Simulated shock waves are placed at the $1/f_0$ or $2/f_0$ timings, but assigned a peak-positive pressure amplitude matching that of the nearest experimentally detected shock wave, thereby illustrating the spectral contribution of *amplitude variance*.
- Interval variance (*black dot*): Simulated shock waves of average peak-positive pressure amplitude are placed at the timings of experimentally detected shock waves, thus demonstrating the effect of *interval variance* in emission timings.
- Both variances (*red dash*): Simulated shock waves are placed at the timings of experimentally detected shock waves and assigned a peak-positive pressure amplitude to match that detected. Comparison of the *both variances* spectrum with the *no variances*, *amplitude* and *interval variance* spectra facilitates identification of the source of all spectral features within the experimental data.

Figure 5(a, b) depicts the amplitudes and timings of the 1st and 13th simulated shock waves, after the reference shock wave detected at $t = 124.148 \mu\text{s}$, for the various synthetic shock wave trains constructed to analyse the f_0 emission data, relative to the respective experimentally detected shock wave (*dark grey, solid*). The profiles of the experimentally detected shock waves are notably wider than those of the simulated counterparts. This is because the initial microbubble position and the microbubble cavitation trajectory during the focused ultrasound exposure (Fig. 2a) is 90–100 μm to the right of the needle hydrophone axis. The shock waves emitted during this activity are therefore incident from an oblique angle, resulting in an increased “spreading effect” over the active element of the hydrophone. The *no variance*, *amplitude variance*, *interval variance* and *both variances* simulated shock waves are similar, reflecting the relatively stable amplitudes and timings of the experimentally detected shock waves emitted in the f_0 regime (Fig. 4a, d). In Figure 5(c, d) are the synthetic spectra for the respective shock wave trains, generated *via* application of a fast Fourier transform to each synthetic shock wave train over the duration of experimental detection, with the spectra of the experimentally detected signal, inclusive of focused ultrasound driving and propagation harmonics (Fig. 1b and Table 1) also presented. The *no variance spectrum* (Fig. 5d, *green dot*) exhibits spectral peaks at nf_0 , with a 0-dB noise floor, consistent with spectral analysis model for periodic shock waves (Song *et al.* 2016). *Amplitude variance*, *interval variance* and *both variances* spectra also feature nf_0 peaks, but decreasing in magnitude at higher frequencies, and with frequency-dependent noise floors each with a maximum value of ~ 40 dB (Fig. 5c). Instrumental noise (Fig. 5d, *brown dot*), however, of ~ 55 dB is seen to account for the noise floor of the spectrum of the experimentally detected signal for this regime.

For the $f_0/2$ data, the reference shock wave (as the first visible in Supplementary Video S4) was detected by the needle hydrophone with the peak-positive pressure amplitude occurring at 127.380 μs . Figure 6a reveals the timings and amplitudes of the 1st simulated shock wave from the various synthetic shock wave trains, relative to the next experimental shock wave after the reference shock wave, detected at 130.315 μs (*blue*), therefore representing an emission interval of 2.935 μs . The peak amplitudes of the simulated shock waves of the *no variance* and *amplitude variance* trains are located 0.046 μs earlier, illustrating the slight temporal offset for the experimentally detected shock wave from “perfect” $2/f_0$ emission timing. Figure 6b is the equivalent representation around the 5th experimentally detected shock wave, demonstrating that in this instance, the “perfect” $2/f_0$ timings of the *no variance* and *amplitude variance*

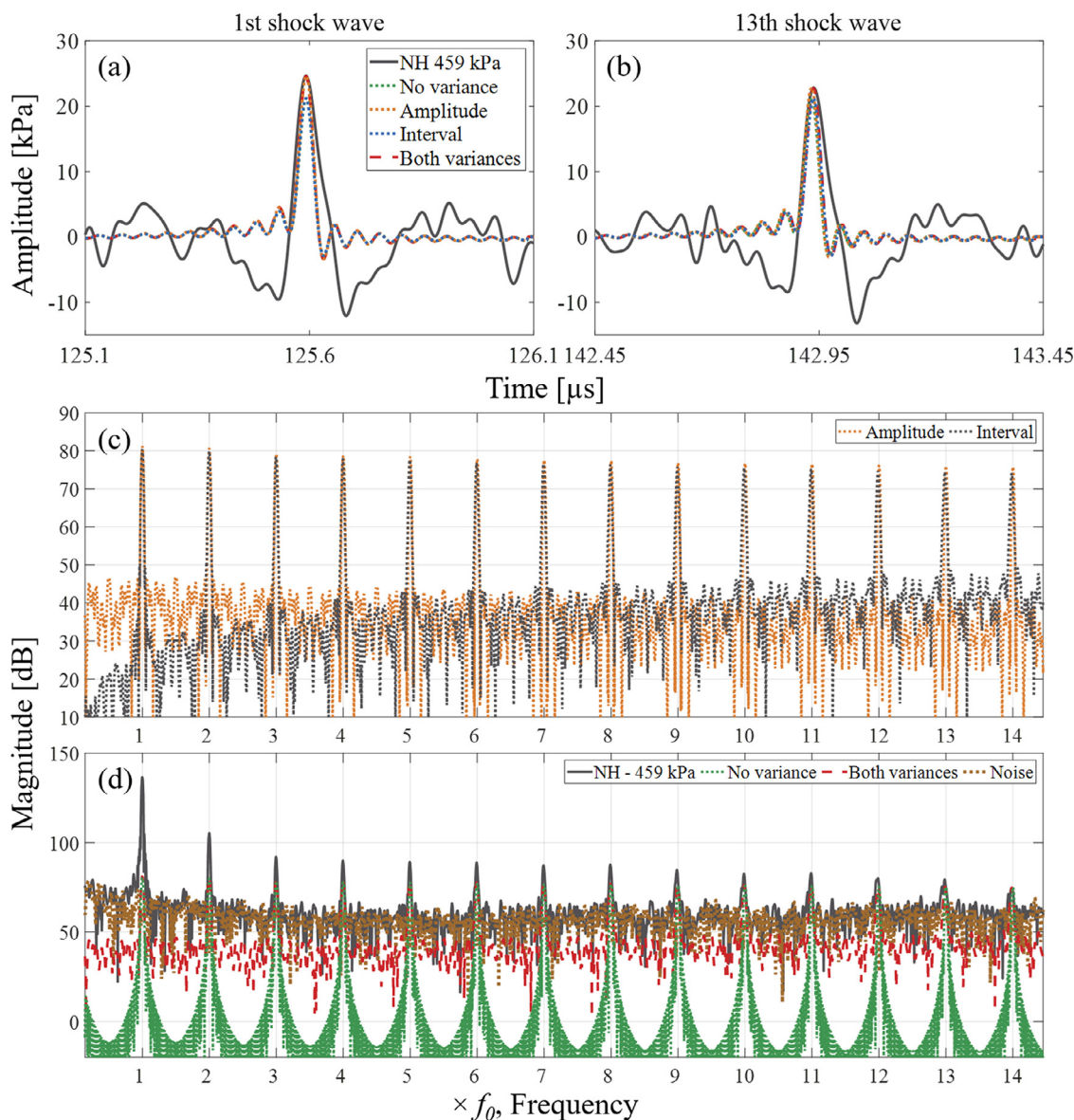


Fig. 5. (a, b) The various synthetic simulated shock wave trains, constructed to analyse the f_0 -shock wave emission regime, for the microbubble cavitation activity driven at a peak-negative pressure of 459 kPa, sampled around the 1st and 13th shock waves after the reference shock wave, detected at 124.148 μ s. (c) *Amplitude variance* and *interval variance* synthetic spectra, revealing spectral peaks at nf_0 , and frequency-dependent noise floors, each with a maximum value of ~ 40 dB. (d) *No variances*, instrumental noise, *both variances* (combining *amplitude variance* and *interval variance*) and the experimental spectra.

synthetic shock wave trains locate the simulated shock waves 0.047 μ s after that experimentally detected. The *no variance* synthetic spectrum (Fig. 6d) of the synthetic shock wave train with simulated shock wave profiles at regular $2/f_0$ timings and constant average peak-positive pressure amplitude exhibits peaks at all $nf_0/2$ with a low noise floor of ~ 15 dB. The *amplitude* and *interval variance* spectra (Fig. 6c) also exhibit $nf_0/2$ peaks, but with notably elevated and frequency-dependent noise floors. The elevation for *interval variance* is more pronounced at higher frequencies due to the relatively small temporal

differences introduced to perfect $2/f_0$ timings, for matching to the experimentally detected shock wave timings. The noise floor of *both variances* (combining *amplitude* and *interval variance*) (Fig. 6d, red dash), over the level of instrumental noise (brown dot), constitutes the broadband component of the microbubble cavitation emission signal, for the $f_0/2$ shock wave regime, driven at PNP = 1.14 MPa. The remaining magnitude deficit across features in both f_0 and $f_0/2$ synthetic spectrum reconstructions may be attributed to shock wave spreading effects across the active element of the needle

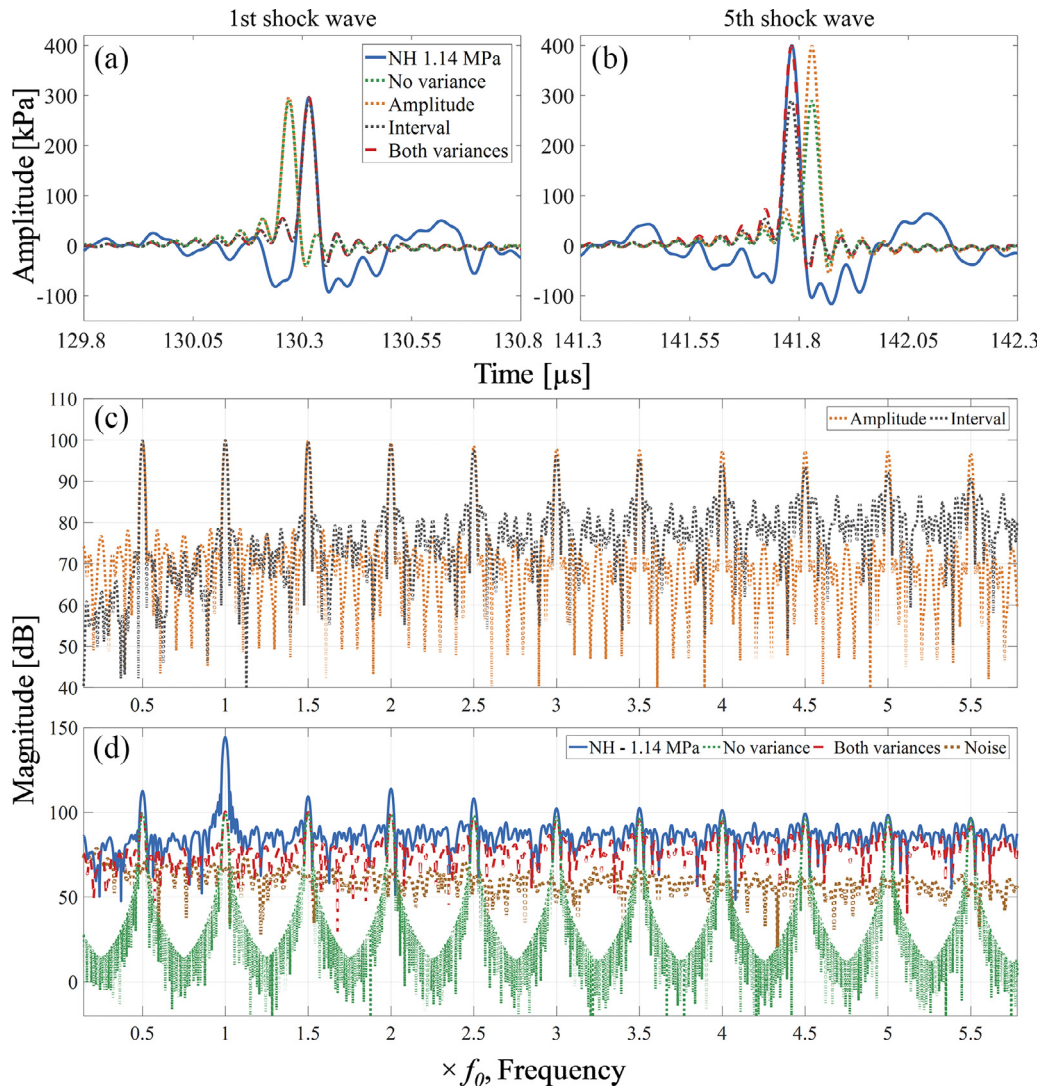


Fig. 6. (a, b) Synthetic simulated shock wave trains, for $f_0/2$ data analysis, sampled around the first and fifth shock waves experimentally detected after the reference shock wave, detected at $127.380 \mu\text{s}$. (c) *Amplitude variance* and *interval variance* spectra, revealing $nf_0/2$ peaks and the respective contributions to the noise floor. (d) *No variances*, instrumental needle hydrophone noise, *both variances* (combining *amplitude variance* and *interval variance*) and the experimental spectra.

hydrophone tip (Song *et al.* 2016) and non-linear propagation components of the focused ultrasound at the respective PNPs (Fig. 1b).

Microbubble cavitation at intermediate PNPs

This section provides experimental data equivalent to those presented for the f_0 and $f_0/2$ shock wave emission regimes, for focused ultrasound driving at intermediate PNPs of 593 and 863 kPa.

Figure 7a (and Supplementary Video S5, online only) represents the minimal degree of fragmentation observed across all experiments, with the fragmentation event occurring at $\sim 104 \mu\text{s}$. Before this, the microbubble appears to cavitate as a single bubble for the initial ~ 27 cycles of the

focused ultrasound burst. Side-view imaging (Fig. 8a; Supplementary Video S6, online only), which was recorded after fragmentation occurred, reveals $\sim f_0$ -shock wave emission at 147.4 and $148.8 \mu\text{s}$ (arrowed red) and some minor deviation from radially symmetric oscillations.

The microbubble driven by a PNP of 863 kPa (Fig. 7b; Supplementary Video S7, online only) exhibits a higher degree of fragmentation, from earlier in the focused ultrasound exposure. As for microbubble cavitation driven at 1.14 MPa, the debris tends to form in the wake of the cloud translation and generally re-merges with the cloud within the cycle. Figure 8b and Supplementary Video S8 (online only) indicate that shock wave emission occurs at both f_0 and $f_0/2$ intervals.

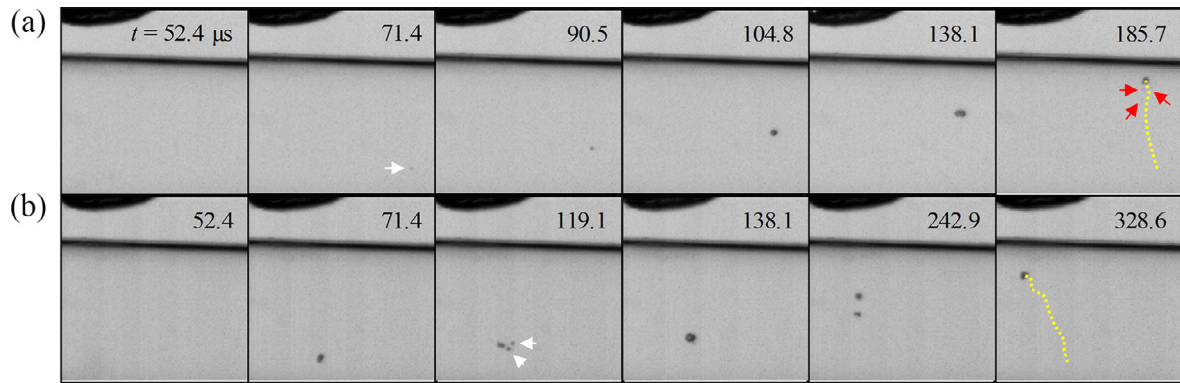


Fig 7. Representative images extracted from a top-view imaging sequence captured at 210 kfps, from $t = 0 \mu\text{s}$ for the duration of the focused ultrasound exposure, of microbubble cavitation activity driven by peak-negative pressures of (a) 593 kPa and (b) 863 kPa. Scale is provided by the $500\text{-}\mu\text{m}$ internal diameter of the capillary. The moment of focused ultrasound generation at the transducer defines $t = 0 \mu\text{s}$, with a propagation time to the capillary of $51.6 \mu\text{s}$.

The acoustic data in Figure 9(a, b) illustrate the shock wave emission characteristics of microbubble cavitation driven by intermediate focused ultrasound PNPs of (a) 593 and (b) 863 kPa. At the lower amplitude, approximately f_0 -shock waves are apparent both before and after the fragmentation event at $\sim 104 \mu\text{s}$, at peak-positive pressure values slightly higher than those emitted during the 459-kPa driving (Fig. 4a). The shock

wave interval plot of Figure 9d (red), however, indicates higher variance in shock wave emission timings, after the fragmentation has occurred. The inset to Figure 9a is time-domain data captured around the moment of microbubble cavitation contact with the capillary wall, at $\sim 210 \mu\text{s}$ (Supplementary Video S5), indicating emissions decrease to instrumental noise or below for the remainder of the focused ultrasound burst.

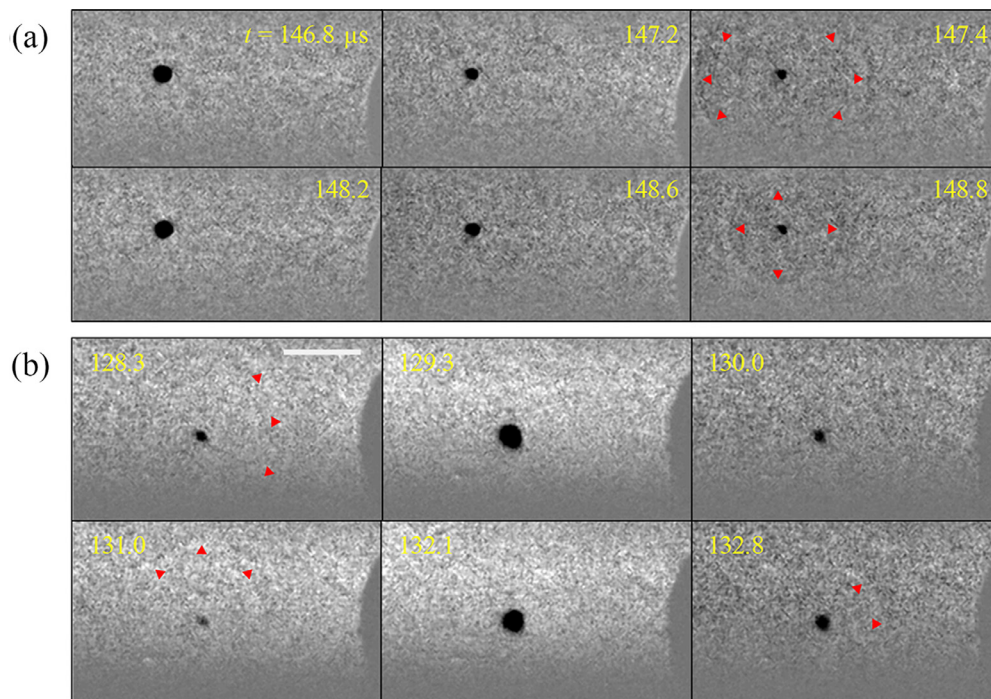


Fig 8. Images extracted from a side-view shadowgraphic sequence at 10 Mfps, from $t = 125 \mu\text{s}$, of the microbubble cavitation activity represented from top-view imaging in Figure 7, at peak negative pressures of (a) 593 kPa and (b) 863 kPa. Images are background-subtracted to enhance shadowgraphic features, including the focused ultrasound driving and bubble collapse shock waves, arrowed red. Bar = $150 \mu\text{m}$; however, the cavitation activity appears larger, as the imaging is purposefully defocused for shadowgraphic capability.

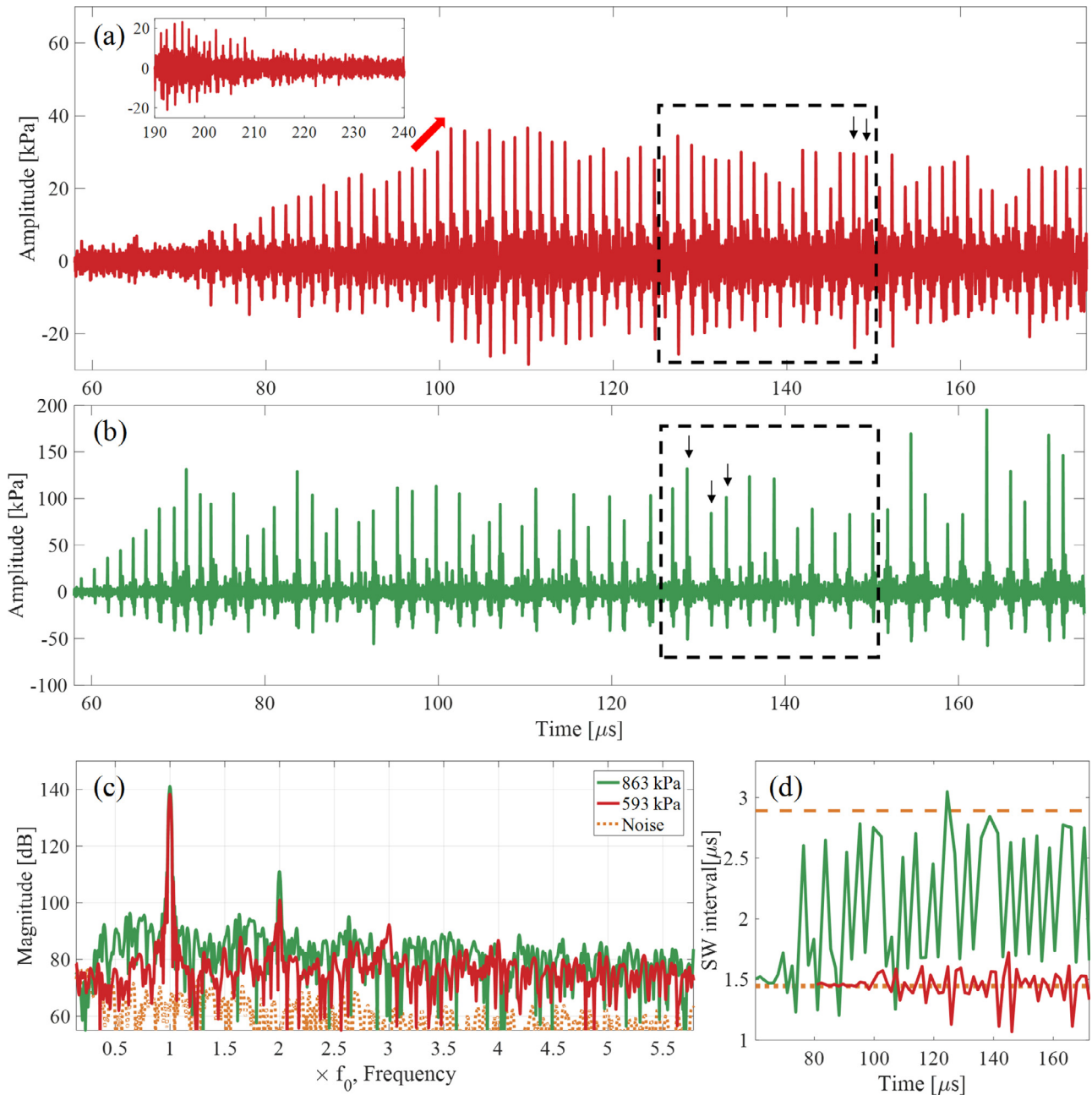


Fig. 9. (a, b) Needle hydrophone data, filtered and deconvolved from 2.4 to 20 MHz, to reveal shock wave content within the microbubble cavitation emission signal, from the activity imaged in Figures 7 and 8 at peak negative pressures of 593 and 863 kPa, respectively. In the inset to (a) are the data from around microbubble cavitation contact with the capillary wall, at $\sim 210 \mu\text{s}$. *Black-dash boxes* correspond to the duration of side-view shadowgraphic imaging, with shock waves *arrowed* in Figure 8(a, b) similarly identified. (c) The spectra of (a) and (b), deconvolved over the full calibration bandwidth, thereby include focused ultrasound driving. The needle hydrophone instrumental noise floor is also depicted (*orange dot*). (d) Variance in shock wave emission times measured from (a) and (b). SW = shock wave.

At the higher-amplitude intermediate driving of PNP = 863 kPa, it can be seen that the microbubble cavitation switches regularly between f_0 - and $f_0/2$ -shock wave emission, also illustrated in Figure 9d (*green*), with a mean period of $2.02 \pm 0.56 \mu\text{s}$ (with

$3 f_0/2 = 2.175 \mu\text{s}$). The spectra for both intermediate driving amplitudes (Fig. 9c) exhibit no clear peaks other than f_0 and $2f_0$ and elevated noise floors relative to needle hydrophone instrumental noise, disproportionately around $f_0/2$, for 863 kPa driving.

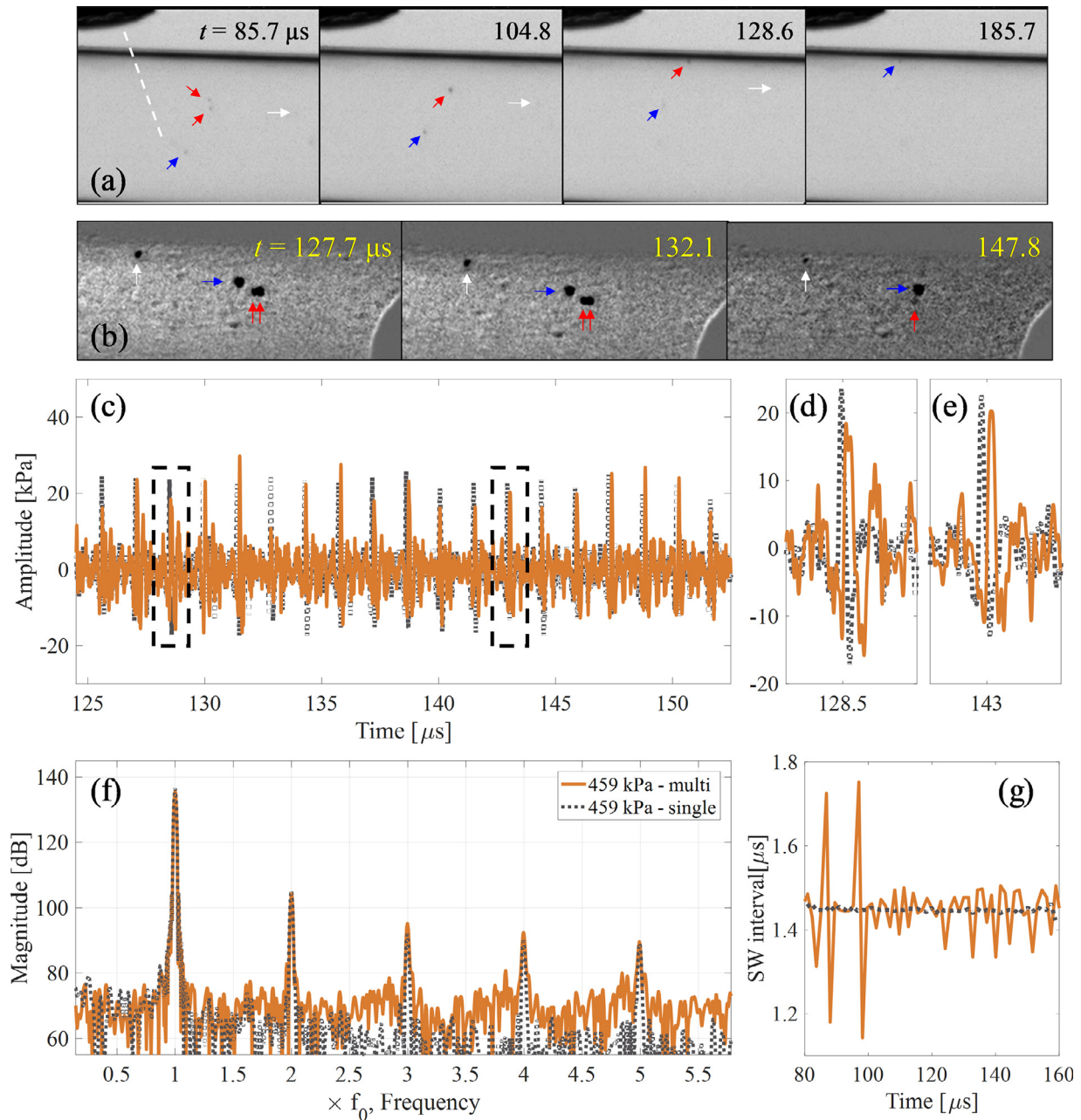


Fig. 10. Representative images extracted from sequences of a multiple-microbubble observation, (a) top-view and (b) side-view, at a peak-negative pressure of 459 kPa. (c–e) Time domain data from the duration of side-view imaging, (f) the spectrum (taken from $t = 58–175 \mu\text{s}$) and (g) apparent shock wave emission interval, all presented relative to equivalent data for single microbubble driven at 459 kPa (dotted black) of Figure 4c.

Multiple microbubble observation

Our primary aim was to collect data sets from single microbubble cavitation events, for ease of reconciling the acoustic emissions directly to the high-speed imaging, and shadowgraphic side-view capture of bubble collapse shock waves, in particular. During the course of repeating experiments to collect data from a relatively isolated microbubble aligned to the needle hydrophone, however, many multiple-microbubble observations were also gathered. As monitoring

of driven microbubble cavitation emissions during therapy will involve detection from many microbubbles (which will also be distributed through the vasculature), we present a summary of a multiple-microbubble data set in this section. The data were collected for focused ultrasound driving of PNP = 459 kPa and, so bear some comparison to the single-microbubble cavitation at this PNP described previously.

Top-view imaging (Figure 10a; Supplementary Video S9, online only) indicates five microbubbles are

initially excited, with the emissions from the three *arrowed red and blue* at $t=85.7 \mu\text{s}$ dominating the acoustic data sampled during side-view imaging (Fig. 10c–g), because of needle hydrophone directivity. The two microbubbles *arrowed red* start cavitating at $\sim 44 \mu\text{m}$ from each other, appear to coalesce within $30 \mu\text{s}$ and contact the capillary wall some $30 \mu\text{s}$ later. Coincidentally, side-view image capture (Fig. 10b; Supplementary Video S10, online only), occurs around the moment of contact. Note, top-view imaging reveals the cavitating bubble *arrowed blue* is $\sim 200 \mu\text{m}$ behind the coalesced bubble, along the axis of side-view imaging. Capillary wall contact is apparent as a cessation of translation, with the amplitude of oscillation diminishing over several cycles of focused ultrasound. Side-view imaging (Fig. 10b) at $132.1 \mu\text{s}$ also suggests that the component cavitation bubbles may not have fully merged during the coalescence. Almost simultaneously, a cavitating bubble near the top of the capillary, and therefore poorly focused in top-view imaging (*arrowed white* in Fig. 10a), also contacts the capillary wall. Although only faintly apparent, this microbubble cavitation gives some confidence that driven cavitation-bubble activity at the top and bottom extremities of the capillary is perceptible in top-view imaging, even at the lowest focused ultrasound driving PNP presented.

The time-domain acoustic data in Figure 1c are laid over the data of the single microbubble cavitation driven at 459 kPa (from Fig. 4a), over the duration of side-view imaging, to facilitate comparison. cursory inspection suggests similarities in terms of f_0 -shock wave emission times, but higher variance in peak-positive pressure amplitude. Closer inspection (Fig. 10d, e), indicates unresolved multiple shock waves apparent as double peaks (d) or broadened full-width half maxima (e). The timings of component shock wave detection from the individual cavitating microbubbles are similar, as the average shock wave propagation speed is similar to that of the focused ultrasound driving each collapse. The spectrum of the detected emission signal features nf_0 peaks, as for the single-microbubble cavitation driven by 459 kPa, but with an elevated noise floor across frequencies $>2.5 \text{ MHz}$, by $\sim 10 \text{ dB}$.

DISCUSSION

These results support periodic bubble collapse-generated shock waves as a mechanistic source of non-linear acoustic emissions from microbubbles, driven below resonance and at parameters typical of those employed for therapy. The period of shock wave emission determines the frequency values at which spectral peaks occur (Song *et al.* 2016), with nf_0 occurring for lower driving

PNPs, for microbubble cavitation emitting f_0 -shock waves on collapse with every compressional phase. The lowest threshold PNP amplitude required to drive microbubble oscillation sufficiently for shock wave generation has not been identified because of the limited spatial resolution of the imaging perspectives, preventing verification of any needle hydrophone data. We did, however, observe f_0 -shock wave emission at a reduced PNP of 385 kPa (data not presented), suggesting that this response regime extends to amplitudes lower than that reported above. At a PNP amplitude of 1.14 MPa, well in excess of the fragmentation threshold, the resulting cavitation cloud exhibits period-doubled oscillations, collapsing sufficiently for shock wave emission only in response to alternate compressional phases, raising spectral peaks at $nf_0/2$. At these higher driving PNPs, the amplitude of the bubble-cloud oscillation becomes sufficiently large that the inertia of the host medium prevents full collapse, with every compressional phase. This behaviour has been reported previously, for single and apparently non-fragmented microbubbles exposed to diagnostic imaging-like frequencies (Chomas *et al.* 2002), but without parallel acoustic detection. Indeed, such incomplete oscillations were identified in early solutions to Rayleigh–Plesset-type equations, for single-bubble oscillation (Borotnikov and Solukhin [1964], as referred to in Neppiras (1980)), and was proposed as a candidate mechanism, amongst others, for subharmonic generation (Neppiras 1980).

Microbubble cavitation behaviour that can contribute to an elevated noise floor in spectra, through broadband emissions, is also investigated. The single, un-fragmented, microbubble cavitation driven at a PNP of 459 kPa generated f_0 -shock waves with the lowest variances, such that the noise floor of the spectrum, between the nf_0 peaks, corresponded to instrumental noise for the detector. For fragmented microbubble cavitation at higher PNPs, more pronounced variance in the shock wave emission interval timings and peak-positive pressure amplitudes effectively redistribute power from the spectral peaks, raising the floor to above instrumental noise. Multiple-microbubble cavitation, driven at the lower PNP amplitude, generated shock waves from multiple sources that were incident to the needle hydrophone tip at approximately the same time, such that similar nf_0 peaks were raised in the spectrum. Differences in arrival time of up to several hundred nanoseconds, for the component shock waves from each source, however, were sufficient to raise the noise floor relative to the emission spectrum for the single-microbubble cavitation, across higher frequencies. We also note that the imaged coalescence event from the multiple-microbubble cavitation observations had no discernible effect on the regime of microbubble cavitation response or the eventual

dissolution of the combined bubble on contact with the capillary wall.

Blood vessel diameters in the brain range from ~ 8 μm for capillaries to several millimeters for the middle cerebral artery, with capillaries far outnumbering larger vessels. The 500- μm internal diameter of the polycarbonate capillary used for this work is therefore only comparable to a limited number of blood vessels in the brain, with smaller capillaries known to significantly suppress microbubble oscillation amplitude (Thomas et al. 2013; Caskey et al. 2006). Moreover, microbubble cavitation *in vivo* will also be influenced by viscosity and the presence of blood cells (Sboros 2008). Further work is required to investigate the effect of reduced capillary diameter on periodic shock waves as the source of non-linear emissions from driven microbubbles. If, however, microbubble cavitation oscillations are suppressed, such that periodic shock waves are not generated as described, raises the possibility that emissions detected during *in vivo* studies may result from a limited number of microbubble cavitation events, in larger blood vessels, and may not necessarily be representative of the microbubble population activity within the vasculature.

To investigate single-microbubble cavitation behaviour, and directly link the non-linear emissions generated to that behaviour, we employed a highly dilute microbubble solution, repeating experiments until single-microbubble cavitation was initiated within the target region, defined by the location of the needle hydrophone tip. Recent debate around safe blood–brain barrier disruption suggests that lower concentrations may be favourable for avoidance of undesirable bio-effects, such as sterile inflammation (Kovacs et al. 2017a, 2017b; McMahon and Hynnen 2017, 2018; Silburt et al. 2017); however, most *in vitro* and *in vivo* experiments will involve detection from many driven microbubbles. We have previously reported on the effects that a distributed two-bubble cavitating system can have on the spectrum of the combined emissions (as recorded with a single-element detector), including spectral windowing that can significantly suppress the key emissions associated with the regime of bubble response (Song et al. 2017). For microbubbles exposed to focused ultrasound in the vasculature, where the resulting microbubble cavitation activity will at least initially be spatially distributed throughout the vessel network, spectral peak suppression in the emissions from neighbouring vessels could be an important and underrecognised effect, which could account for some of the variability reported for *in vivo* studies (Gorick et al. 2018).

Although the experiments described were intended primarily for identification of the mechanistic source of non-linear emissions, during microbubble cavitation under subresonant focused ultrasound exposure, several

of the observations may also have relevance for the mechanisms of tissue disruption. In particular, the consistent observation that microbubble cavitation in f_0 -shock wave emission regimes did not survive contact with the capillary wall could be significant. In contrast, the microbubble cavitation driven at 1.14 MPa, responding in the $f_0/2$ regime, endures after contact and continues to translate along the inner surface. If this is indicative of microbubble cavitation in vasculature, then the sustained mechanical activity in contact with the endothelial layer at higher PNP amplitudes could explain the more aggressive, often irreversible, bio-effects associated with subharmonic emissions (O'Reilly and Hynnen 2012; Jones et al. 2018). Beyond physical contact, the role of bubble collapse shock waves for tissue disruption is a topic of ongoing research, with a thorough review recently available (Lopez-Marin et al. 2018). The directivity of the 0.2-mm needle hydrophone used, and its close proximity to the capillary, mean the peak-positive pressure amplitudes of the shock wave measurements reported are sensitive to the precise bubble location, relative to the needle tip, including as a result of translation of the activity during the focused ultrasound exposure. It is, however, notable that the shock waves emitted in the $f_0/2$ regime are an order of magnitude greater than those emitted during f_0 -emission activity. Clearly, further work is required to verify these potential mechanisms *in vivo*.

In reports of applications of acoustic cavitation, generally, there is a tendency to classify activity as stable or inertial, despite existing recognition that this categorisation is likely an oversimplification (Ashokkumar 2011; Leighton 1994), including for contrast agent microbubbles (Church and Carstensen 2001), with many more subcategories required for a full description. In studies developing pre-clinical applications of focused ultrasound and microbubbles for therapy in particular, stable cavitation is often associated with harmonic emissions, broadband noise with inertial activity and subharmonic emission as a signal indicative of transitioning between the categories (the “upper limit” of stable cavitation). The work presented here further suggests that this conventional categorisation is indeed inadequate and, perhaps, unhelpful. Harmonic and subharmonic emissions are both mediated by collapse-generated shock waves, a conventionally inertial effect. Moreover, elevated noise can result from variance in shock wave emission timings and peak-positive amplitudes, occurring after a fragmentation event under driving at intermediate PNP amplitudes, or from multiple-microbubble cavitation driven by an f_0 -shock wave emission regime PNP.

The results presented do not preclude the possibility of other mechanisms of non-linear emissions, such as

non-spherical oscillations, within a population of microbubbles exposed to focused ultrasound, for example, some of which will be excited by lower pressure amplitudes, outside or at the periphery of the focal region. The imaging FOVs for the current work, necessary to accommodate radiation force-induced translation and capturing shock wave emission, have associated spatial resolutions inadequate for investigating the interface of the bubble boundary. However, microbubble cavitation responding to an ultrasound exposure with the strong collapse phases necessary for periodic shock wave emission, including fragmentation events at higher amplitudes, is unlikely to simultaneously sustain non-spherical oscillation activity.

Finally, from all experiments performed, we note that we did not observe any variation in periodic shock wave emission behaviour that might be attributable to the initial microbubble properties, such as quiescent equilibrium radius. As described under Methods, the resolution of both imaging perspectives is inadequate for resolving microbubbles before focused ultrasound excitation, however, more than 100 observations of microbubble cavitation activity were taken at each of the PNP amplitudes reported, the majority of which consist of multiple-microbubble cavitation events and single-microbubble cavitation events not sufficiently aligned to the needle hydrophone tip for synthetic signal reconstruction. Nonetheless, all observed microbubble cavitation displayed the general regime of periodic shock wave emission characteristics described above, in accordance with the PNP of the focused ultrasound exposure. This is supported through comparison of the single-microbubble and multiple-microbubble cavitation observations, both driven at a PNP of 459 kPa, for which all component cavitation events collapse repeatedly at f_0 and thereby emit f_0 -shock waves. Assuming that across all observations for each PNP investigated, a representative cross section of the SonoVue microbubble subpopulation, of initial diameter $<5 \mu\text{m}$, has been sampled, suggests that the initial microbubble serves as a nucleus, with the acoustics dictating the subsequent cavitation activity. This is in contrast to the strong dependence of spherical subharmonic response in microbubbles excited at higher frequencies and lower driving amplitudes, for example, which was observed in $\sim 50\%$ of microbubbles and thought to depend critically on shell parameters (Sijl *et al.* 2010).

CONCLUSIONS

The role of periodic bubble collapse-generated shock waves within the acoustic emissions from therapeutically driven contrast agent microbubbles is evaluated. All non-linear spectral features, including harmonic, subharmonic

and broadband emissions, can be accounted for through periodic shock wave characteristics, according to the pressure amplitude of the driving. Further research is required to validate these findings for *in vivo* microbubble cavitation for tissue disruption and drug delivery.

Acknowledgments—The research leading to these results has received funding from the European Research Council under the European Union's Seventh Framework Programme (FP/2007-2013)/ERC Grant Agreement No. 336189 (TheraCav). We also acknowledge support from EPSRC network ThUNDDAR, in collaboration with Dr. James McLaughlan at the University of Leeds, UK. The authors are very grateful to Mr. Ewan Russell for preparing graphics associated with this work, Mr. Kristoffer Johansen for motivation and Professors Tony Gachagan and Sandy Cochran for support.

SUPPLEMENTARY MATERIALS

Supplementary material associated with this article can be found in the online version at [doi:10.1016/j.ultrasmedbio.2019.04.005](https://doi.org/10.1016/j.ultrasmedbio.2019.04.005).

REFERENCES

- Ashokkumar M. The characterization of acoustic cavitation bubbles—An overview. *Ultrason Sonochem* 2011;18:864–872.
- Caskey CF, Kruse DE, Dayton PA, Kitano TK, Ferrara KW. Microbubble oscillation in tubes with diameters of 12, 25, and 195 microns. *Appl Phys Lett* 2006;88 033902.
- Caskey CF, Steiger Sm, Qin S, Dayton PA, Ferrara KW. Direct observations of ultrasound microbubble contrast agent interaction with the microvessel wall. *J Acoust Soc Am* 2007;122:1191–1200.
- Chen H, Brayman AA, Kreider W, Bailey MR, Matula TJ. Observations of translation and jetting of ultrasound-activated microbubbles in mesenteric microvessels. *Ultrasound Med Biol* 2011a;37:2139–2148.
- Chen H, Kreider W, Brayman AA, Bailey MR, Matula TJ. Blood vessel deformations on microsecond time scales by ultrasonic cavitation. *Phys Rev Lett* 2011b;106 034301.
- Chomas J, Dayton PA, May D, Ferrara KW. Nondestructive subharmonic imaging. *IEEE Trans Ultrason Ferroelectr Freq Control* 2002;49:883–892.
- Church CC, Carstensen EL. “Stable” inertial cavitation. *Ultrasound Med Biol* 2001;27:1435–1437.
- de Jong N, Emmer M, Chin CT, Bouakaz A, Mastik F, Lohse D, Versluis M. “Compression-only” behavior of phospholipid-coated contrast bubbles. *Ultrasound Med Biol* 2007;33:653–656.
- Dollet B, van der Meer SM, Garbin V, de Jong N, Lohse D, Versluis M. Nonspherical oscillations of ultrasound contrast agent-microbubbles. *Ultrasound Med Biol* 2008;34:1465–1473.
- Ferrara KW, Pollard R, Borden M. Ultrasound microbubble contrast agents: Fundamentals and application to gene and drug delivery. *Annual Rev Biomed Eng* 2007;9:415–447.
- Gorick GM, Sheybani ND, Curley CT, Price RJ. Listening in on the microbubble crowd: Advanced acoustic monitoring for improved control of blood–brain barrier opening with focused ultrasound. *Theranostics* 2018;8:2988–2991.
- Johansen K, Song JH, Johnston K, Prentice P. Deconvolution of acoustically detected bubble-collapse shock waves. *Ultrasonics* 2017;73:144–153.
- Johnston K, Prentice P, Gerold B. Cavitation cloud translation in focused ultrasound: Primary radiation force-mediated effects at varying intensity. *Proc IEEE Int Ultrason Symp* 2014;61–64.
- Jones RM, Deng LL, Leung K, McMahon D, O'Reilly MA, Hynynen K. Three-dimensional transcranial microbubble imaging for guiding volumetric ultrasound-mediated blood–brain barrier opening. *Theranostics* 2018;8:2909–2926.

- Kovacs ZI, Kim S, Jikaria N, Milo B, Lewis BK, Bresler M, Burks SR, Frank JA. Disrupting the blood–brain barrier by focused ultrasound induces sterile inflammation. *Proc Natl Acad Sci* 2017a;114:E75–E84.
- Kovacs ZI, Burks SR, Frank JA. Concerning sterile inflammation following focused ultrasound and microbubbles in the brain. *Proc Natl Acad Sci* 2017b;114:E6737–E6738.
- Kreider W, Crum LA, Bailey MR, Sapozhnikov OA. A reduced-order, single-bubble cavitation model with applications to therapeutic ultrasound. *J Acoust Soc Am* 2011;130:3511–3530.
- Kudo N. A simple technique for visualizing ultrasound fields without Schlieren optics. *Ultrasound Med Biol* 2015;41:2071–2081.
- Lajoie G, Luan Y, Gelderblom E, Dollet B, Mastik F, Dewitte H, Lentacker I, de Jong N, Versluis M. Non-spherical oscillations drive the ultrasound-mediated release from targeted microbubbles. *Commun Phys* 2018;1:22.
- Leighton T. *The acoustic bubble*. London: Academic Press; 1994. p. 413–524.
- Lipsman N, Meng Y, Bethune AJ, Huang Y, Lam B, Masellis M, Herrman N, Heyn C, Aubert I, Boutet A, Smith GS, Hynynen K, Black SE. Blood–brain barrier opening in Alzheimer’s disease using MR-guided focused ultrasound. *Nat Commun* 2018; 9:2336.
- Lopez-Marin LM, Rivera AL, Fernandez F, Loske AM. Shock wave-induced permeabilization of mammalian cells. *Phys Life Rev* 2018;26/27:1–38.
- McDannold N, Vykhodtseva N, Hynynen K. Targeted disruption of the blood–brain barrier with focused ultrasound: Association with cavitation activity. *Phys Med Biol* 2006;51:793–807.
- McMahon D, Hynynen K. Acute inflammatory response following increased blood–brain barrier permeability induced by focused ultrasound is dependent on microbubble dose. *Theranostics* 2017;7:3989–4000.
- McMahon D, Hynynen K. Concerning acute inflammatory response following focused ultrasound and microbubbles in the brain. *Theranostics* 2018;8:2249–2250.
- Neppiras E. Acoustic cavitation. *Phys Rep* 1980;61:159–251.
- O’Reilly MA, Hynynen K. Blood–brain barrier: Real-time feedback-controlled focused ultrasound disruption by using an acoustic emissions-based controller. *Radiology* 2012;263:96–106.
- Prentice P, Cuschieri A, Dholakia K, Prausnitz M, Campbell P. Membrane disruption by optically controlled microbubble cavitation. *Nat Phys* 2005;1:107–110.
- Sboros V. Response of contrast agents to ultrasound. *Adv Drug Deliv Rev* 2008;60:1117–1136.
- Schneider M. Characteristics of SonoVue™. *Echocardiography* 1999;16:743–746.
- Sijl J, Overvelde M, Dollet B, Garbin V, Rozerndal T, de Jong N, Lohse D, Versluis M. Subharmonic behavior of phospholipid-coated ultrasound contrast agent microbubbles. *J Acoust Soc Am* 2010;128 3239–2352.
- Sijl J, Overvelde M, Dollet B, Garbin V, de Jong N, Lohse D, Versluis M. “Compression-only” behavior: A second-order nonlinear response of ultrasound contrast agent microbubbles. *J Acoust Soc Am* 2011;129:1729–1739.
- Silburt J, Lipsman N, Aubert I. Disrupting the blood-brain barrier with focused ultrasound: Perspectives on inflammation and regeneration. *Proc Natl Acad Sci USA* 2017;114:E6735–E6736.
- Song J, Johansen K, Prentice P. An analysis of the acoustic cavitation noise spectrum: The role of periodic shock waves. *J Acoust Soc Am* 2016;140:2494–2505.
- Song J, Johansen K, Prentice P. Covert cavitation: Spectral peak suppression in the acoustic emissions from spatially configured nucleations. *J Acoust Soc Am* 2017;141:EL216–EL221.
- Sun T, Zhnag YZ, Power C, Alexander PM, Sutton JT, Aryal M, Vykhodtseva N, Miller EL, McDannold NJ. Closed-loop control of targeted ultrasound drug delivery across the blood–brain/tumor barriers in a rat glioma model. *Proc Natl Acad of Sci USA* 2017;114:E10281–E10290.
- Thomas DH, Sboros V, Emmer M, Vos H, de Jong N. Microbubble oscillations in capillary tubes. *IEEE Trans Ultrason Ferroelectr Freq Control* 2013;60:105–114.
- van der Meer SM, Versluis M, Lohse D, Chin CT, Bouakaz A, de Jong N. The resonance frequency of SonoVue™. *Proc IEEE Int Ultrason Symp* 2004;343–345.
- van Wamel A, Kooiman K, Hartevelde M, Emmer M, ten Cate FJ, Versluis M, de Jong N. Vibrating microbubbles poking individual cells: Drug transfer into cells via sonoporation. *J Controlled Release* 2006;112:149–155.
- Versluis M, Goertz DE, Palanchon P, Heitman IL, van der Meer SM, Dollet B, de Jong N, Lohse D. Microbubble shape oscillations excited through ultrasonic parametric driving. *Phys Rev E* 2010;82(2) 026321.
- Wu SY, Tung YS, Marquet F, Downs ME, Sanchez CS, Chen CC, Ferrara V, Konofagou E. Transcranial cavitation detection in primates during blood–brain barrier opening—A performance assessment study. *IEEE Trans Ultrason Ferroelectr Freq Control* 2014;61:966–978.